Supporting Information

Synergistic Promotion of Transition Metal Ion-exchange in TiO$_2$ Nanoarray-based Monolithic Catalysts for Selective Catalytic Reduction of NO$_x$ with NH$_3$

Xingxu Lu[a,b], Yanliu Dang[b], Meilin Li[c], Chunxiang Zhu[a,b], Fangyuan Liu[b], Wenxiang Tang[a,b], Junfei Weng[a,b], Mingyue Ruan[a], Steven L. Suib[b,c], Pu-Xian Gao[a,b,*]

[a] Department of Materials Science and Engineering, University of Connecticut, Storrs, CT 06269, USA

[b] Institute of Materials Science, University of Connecticut, Storrs, CT 06269, USA

[c] Department of Chemistry, University of Connecticut, Storrs, CT 06269, USA

* Email: puxian.gao@uconn.edu

KEYWORDS: NH$_3$-SCR; TiO$_2$; Nanoarray; NO$_x$ abatement; Transition metal oxides; Ion-exchange; Aftertreatment; Monolithic catalyst.

1. Experimental Procedures

1.1 Preparation of LPT nanoarrays

The LPT nanoarrays were integrated onto the commercial cordierite honeycombs via a facile microwave-assisted hydrothermal method introduced in our previous work.[1] Before to the synthesis, the as-cleaned cordierite monoliths were seeded using a TiO_2 polymeric sol (0.025 mol/L) followed by calcination. The seeded substrates (5 cm × 5 cm × 2 cm) were then soaked into the solution containing 10.5 mL hydrochloride acid (HCl, 37%, Sigma-Aldrich), 9 mL titanium (III) chloride ($TiCl_3$, 20% w/v solution in 2M HCl acid, Acros Organics™) and 45 mL hydrogen peroxide (H_2O_2, 30%, SIGMA-ALDRICH) in 555 mL deionized (DI) water with the channels perpendicular to the beaker bottom. The hydrothermal synthesis was carried out at 90 °C for 60 min in a BP-125 laboratory microwave (Microwave Research & Applications, Inc.) until the color of the reactant solution turned from deep red to yellow with no more bubbles emerging from the channels. The LPT nanoarrays were rinsed with DI water and dried in oven at 90 °C overnight.

1.2 Preparation of transition metal doped TiO_2 nanoarrays

The transition metal elements were firstly loaded onto the LPT nanoarrays through an ion-exchange process. The LPT nanoarray rooted honeycomb was cut into 2 cm^3 blocks and soaked into the solution containing proper amounts of transition metal precursors, including NH_4VO_3, $Cr(NO_3)_3 \cdot 9H_2O$, $Mn(NO_3)_2 \cdot 4H_2O$, $Fe(NO_3)_3 \cdot 9H_2O$, $Co(NO_3)_2 \cdot 6H_2O$, $Ni(NO_3)_2 \cdot 6H_2O$, $Cu(NO3)2 \cdot 3H2O$, $La(NO_3)_3 \cdot 6H_2O$, $Ce(NO_3)_3 \cdot 6H_2O$. The capped vials were kept in an oven at 80 °C for 12 h, and then the

solution was evaporated at 80 °C until dry. Upon most of the solution had been evaporated, the substrates were flipped every 15-20 min to enhance the uniformity. Finally, the sample was calcined at 500°C for 2 hours, during which, the LPT nanoarrays were converted into anatase TiO_2 structure, resulting the TiO_2 nanoarray supported transition metal catalysts (X/TNA). More specifically, the standard solution containing the precursors with a concentration of 1g transition metal element per liter DI water were prepared. Meanwhile, the LPT nanoarray rooted honeycomb samples were all cut into standard cubes of 2 cm^3. Therefore, the amount of transition metal elements for each sample can be calculated according to the designed loading amount. For example, for the monometallic 100Mn/TNA sample, it contains 100g Mn/ft^3 of the substrate. For a cubic honeycomb sample of 2 cm^3, it is 7.06293e-5 ft^3 in volume, so it requires 7.06293e-3g Mn element in the solution. Therefore, the 100Mn/TNA sample needs 7.06293 ml standard solution. All the mono-, bi- and tri-metallic samples were prepared in this way.

The contents of the prepared catalysts are summarized in **Table S1**.

1.3 Catalyst composition

Table S1. Composition information of the samples prepared in the present work.

ID	Notation	Metal loading
Mono-metallic		
1-1	50V/TNA	50g V/ft^3
1-2	50Cr/TNA	50g Cr/ft^3
1-3	50Mn/TNA	50g Mn/ft^3
1-4	50Fe/TNA	50g Fe/ft^3
1-5	50Co/TNA	50g Co/ft^3

1-6	50Ni/TNA	50g Ni/ft^3	
1-7	50Cu/TNA	50g Cu/ft^3	
1-8	50La/TNA	50g La/ft^3	
1-9	50Ce/TNA	50g Ce/ft^3	
3-3	100Mn/TNA	100g Mn/ft^3	
3-7	100Cu/TNA	100g Cu/ft^3	
3-9	100Ce/TNA	100g Ce/ft^3	
11-1	50Mn/TNA	50g Mn/ft^3	
11-2	100Mn/TNA	100g Mn/ft^3	
11-3	200Mn/TNA	200g Mn/ft^3	
Bi-metallic			
2-1	50-2V-5Mn/TNA	50g (V, Mn)/ft^3	V/Mn=2/5
2-2	50-2Cr-5Mn/TNA	50g (Cr, Mn)/ft^3	Cr/Mn=2/5
2-4	50-2Fe-5Mn/TNA	50g (Fe, Mn)/ft^3	Fe/Mn=2/5
2-5	50-2Co-5Mn/TNA	50g (Co, Mn)/ft^3	Co/Mn=2/5
2-6	50-2Ni-5Mn/TNA	50g (Ni, Mn)/ft^3	Ni/Mn=2/5
2-7	50-2Cu-5Mn/TNA	50g (Cu, Mn)/ft^3	Cu/Mn=2/5
2-8	50-2La-5Mn/TNA	50g (La, Mn)/ft^3	La/Mn=2/5
2-9	50-2Ce-5Mn/TNA	50g (Ce, Mn)/ft^3	Ce/Mn=2/5
4-7	100-2Cu-5Mn/TNA	100g (Cu, Mn)/ft^3	Cu/Mn=2/5
4-9	100-2Ce-5Mn/TNA	100g (Ce, Mn)/ft^3	Ce/Mn=2/5
5-7	100-Cu-Mn/TNA	100g (Cu, Mn)/ft^3	Cu/Mn=1/1
5-9	100-Ce-Mn/TNA	100g (Ce, Mn)/ft^3	Ce/Mn=1/1
6-7	100-5Cu-2Mn/TNA	100g (Cu, Mn)/ft^3	Cu/Mn=5/2
6-9	100-5Ce-2Mn/TNA	100g (Ce, Mn)/ft^3	Ce/Mn=5/2
Tri-metallic			
8-1	50-Cu-Ce-Mn/TNA	50g (Cu, Ce, Mn)/ft^3	Ce/Cu/Mn=1/1/1
8-2	100-Cu-Ce-Mn/TNA	100g (Cu, Ce, Mn)/ft^3	Ce/Cu/Mn=1/1/1
8-3	200-Cu-Ce-Mn/TNA	200g (Cu, Ce, Mn)/ft^3	Ce/Cu/Mn=1/1/1
9-1	50-Cu-Ce-5Mn/TNA	50g (Cu, Ce, Mn)/ft^3	Ce/Cu/Mn=1/1/5
9-2	100-Cu-Ce-5Mn/TNA	100g (Cu, Ce, Mn)/ft^3	Ce/Cu/Mn=1/1/5
9-3	200-Cu-Ce-5Mn/TNA	200g (Cu, Ce, Mn)/ft^3	Ce/Cu/Mn=1/1/5
10-1	50-Cu-Ce-10Mn/TNA	50g (Cu, Ce, Mn)/ft^3	Ce/Cu/Mn=1/1/10

| 10-2 | 100-Cu-Ce-10Mn/TNA | 100g (Cu, Ce, Mn)/ft^3 | Ce/Cu/Mn=1/1/10 |
| 10-3 | 200-Cu-Ce-10Mn/TNA | 200g (Cu, Ce, Mn)/ft^3 | Ce/Cu/Mn=1/1/10 |

1.4 Details of H$_2$-TPR and NO/NH$_3$ TPD

Hydrogen temperature programmed reduction (H2-TPR) was carried out in a ChemiSorb 2720 Pulse Chemisorption System equipped with a TCD detector. Each sample was heated to 550 °C in the 5% O$_2$/N$_2$ for 1 h followed by cooling to room temperature before the test. The H$_2$-TPR was conducted from the 30 to 800 °C at a heating rate of 10 °C/min under 40 sccm 4% H$_2$/N$_2$. The H$_2$ consumption was calculated from the calibration by Copper (II) oxide (CuO, SIGMA-ALDRICH) tested under the same conditions.

Temperature Programmed Desorption (TPD) measurements were performed using a fixed-bed tube reactor, and a Fourier transform infrared spectrometer (FTIR, ThermoFisher Nicolet 6700) equipped with a 2 m path length gas cell (250 mL) was employed to monitor the concentrations of NO, NO$_2$, N$_2$O, and NH$_3$ at the exit. The samples were pretreated in 5 vol.% O$_2$/N$_2$ at 550 °C for 1 h and then cooled to 50 °C before each test. For NH$_3$-TPD, the samples were firstly flushed in 500 ppm NH$_3$/N$_2$ flow (300 sccm) at 50 °C for 1 h, and then the physiosorbed NH$_3$ was removed by purging in N$_2$ (300 sccm) at 50 °C until no NH3 was detected. Subsequently, the catalyst was heated in N$_2$ (300 sccm) from 50 °C to 650 °C with a ramp of 10 °C/min for the NH$_3$ desorption. For NO TPD, feed gas was changed to 500 ppm NO/N$_2$ flow (300 sccm), and the temperature was programmed in the same way as the NH$_3$ TPD.

1.5 Details of catalyst stability tests

The stability tests were conducted using the performance testing conditions and kept at

220 and 315 °C for 50 h, respectively. The composition of exit gases (i.e., NO, NH$_3$, NO$_2$, and N$_2$O) were continuously analyzed by an online FTIR. The sulfur poisoning effects on the catalyst performance were also evaluated following USDRIVE's protocol,[2] in which the catalyst was exposed to 5 ppm SO$_2$ added to the feed gas stream at 300 °C for 5 h. A total sulfur exposure level of 1 g sulfur per liter of catalyst was estimated following this exposure condition. After sulfur exposure, SO$_2$ was removed from the feed and the sample was cooled to 100 °C, from which point the catalyst performance was evaluated following the normal procedure.

2. Results and Discussion

2.1 Catalytic performance tests
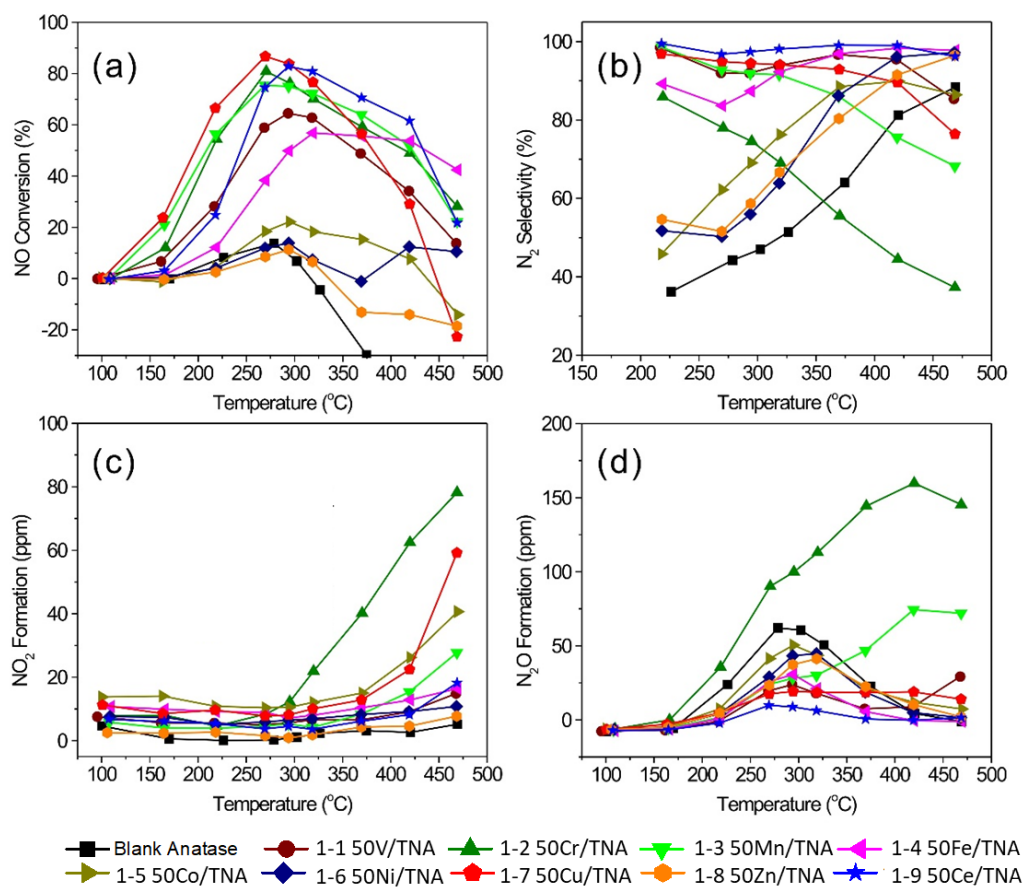
Figure S1. (a) NO conversion, (b) N_2 selectivity, (c) NO_2 formation and (d) N_2O formation of monometallic TiO_2 nanoarray (TNA) based monolithic catalysts.
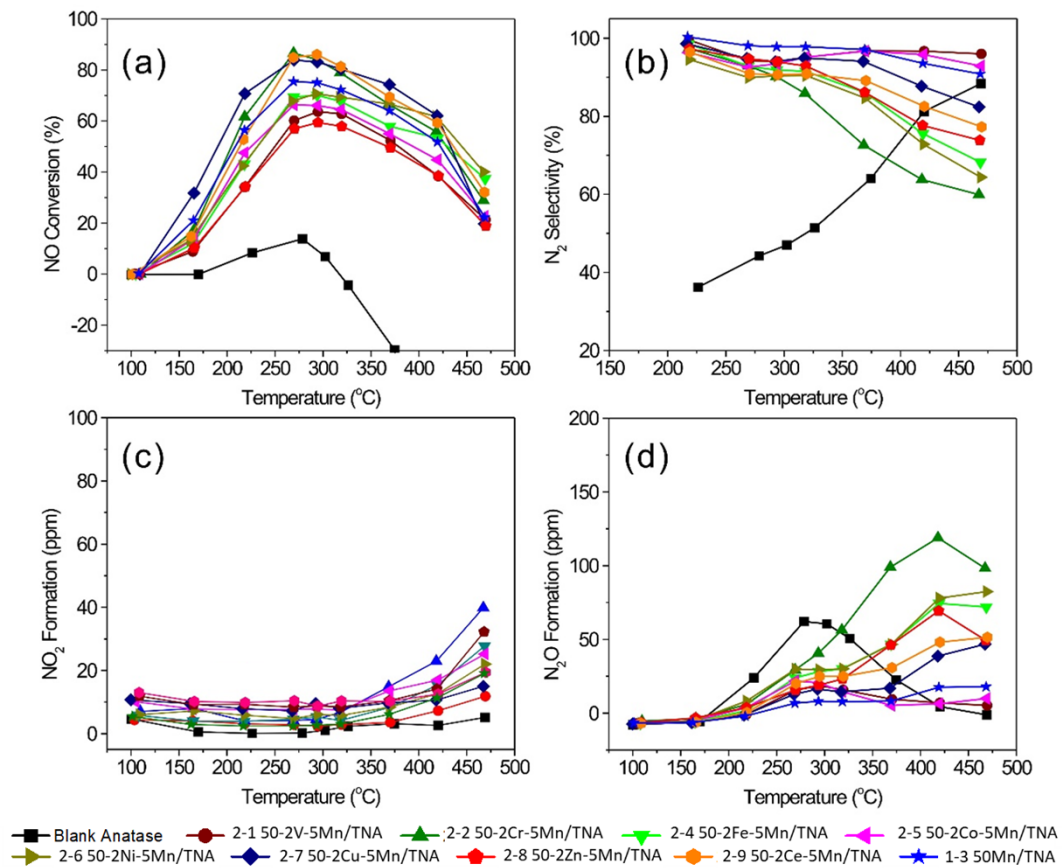
Figure S2. (a) NO conversion, (b) N$_2$ selectivity, (c) NO$_2$ formation and (d) N$_2$O formation of the bimetallic TiO$_2$ nanoarray (TNA) based monolithic catalysts.
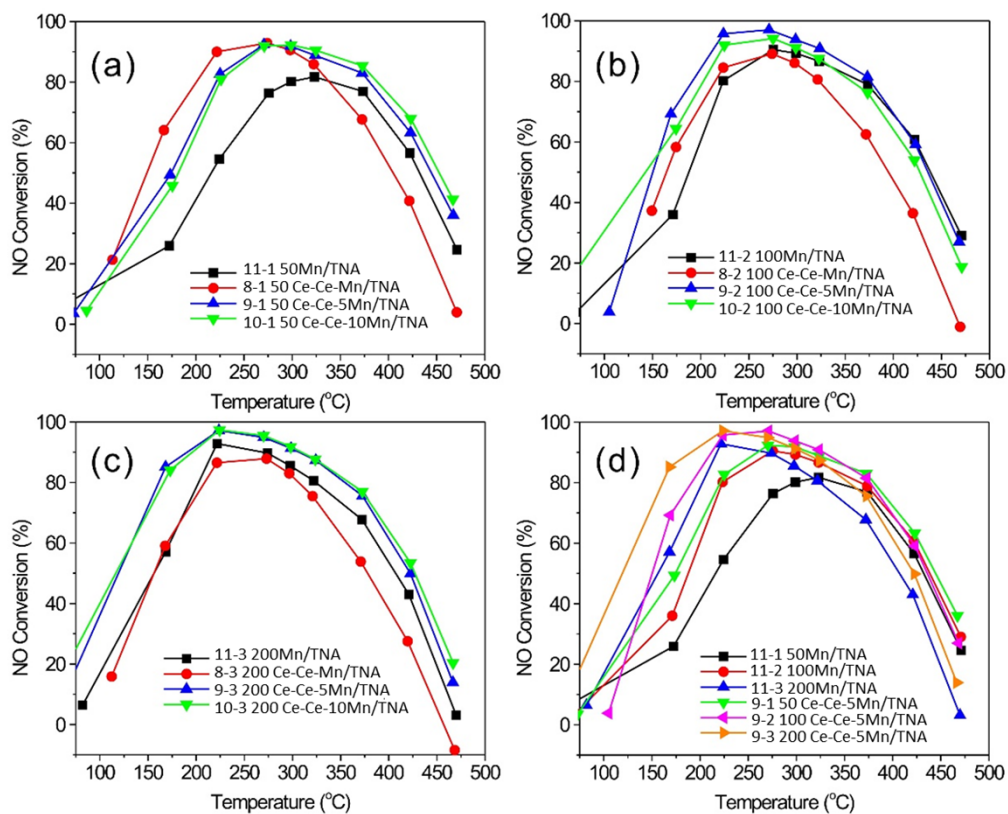
Figure S3. Catalytic performance of the trimetallic catalysts towards NO oxidation.
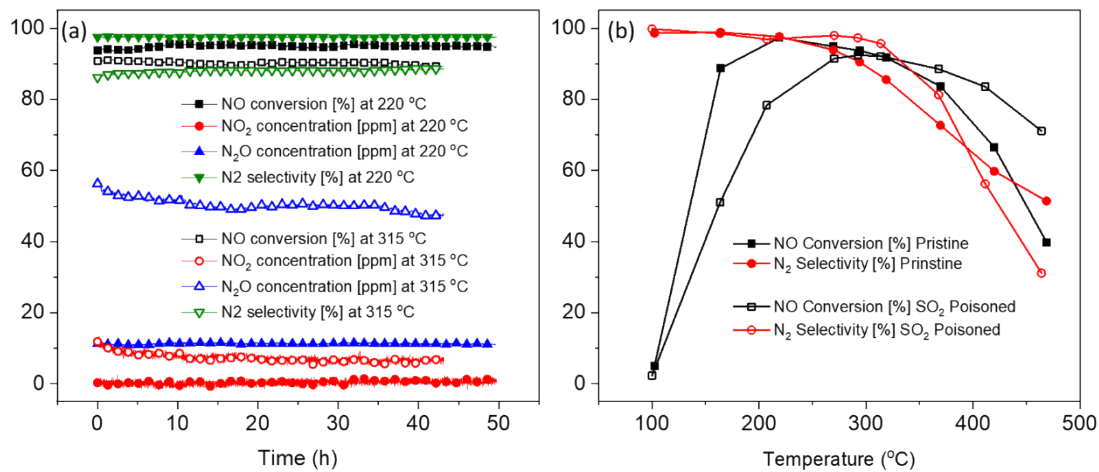

Figure S4. (a) Stability tests at 220 °C (solid symbols) and 315 °C (solid symbols) and

the (b) Sulfur poisoning resistance tests over the trimetallic Cu-Ce-5Mn/TNA catalyst.
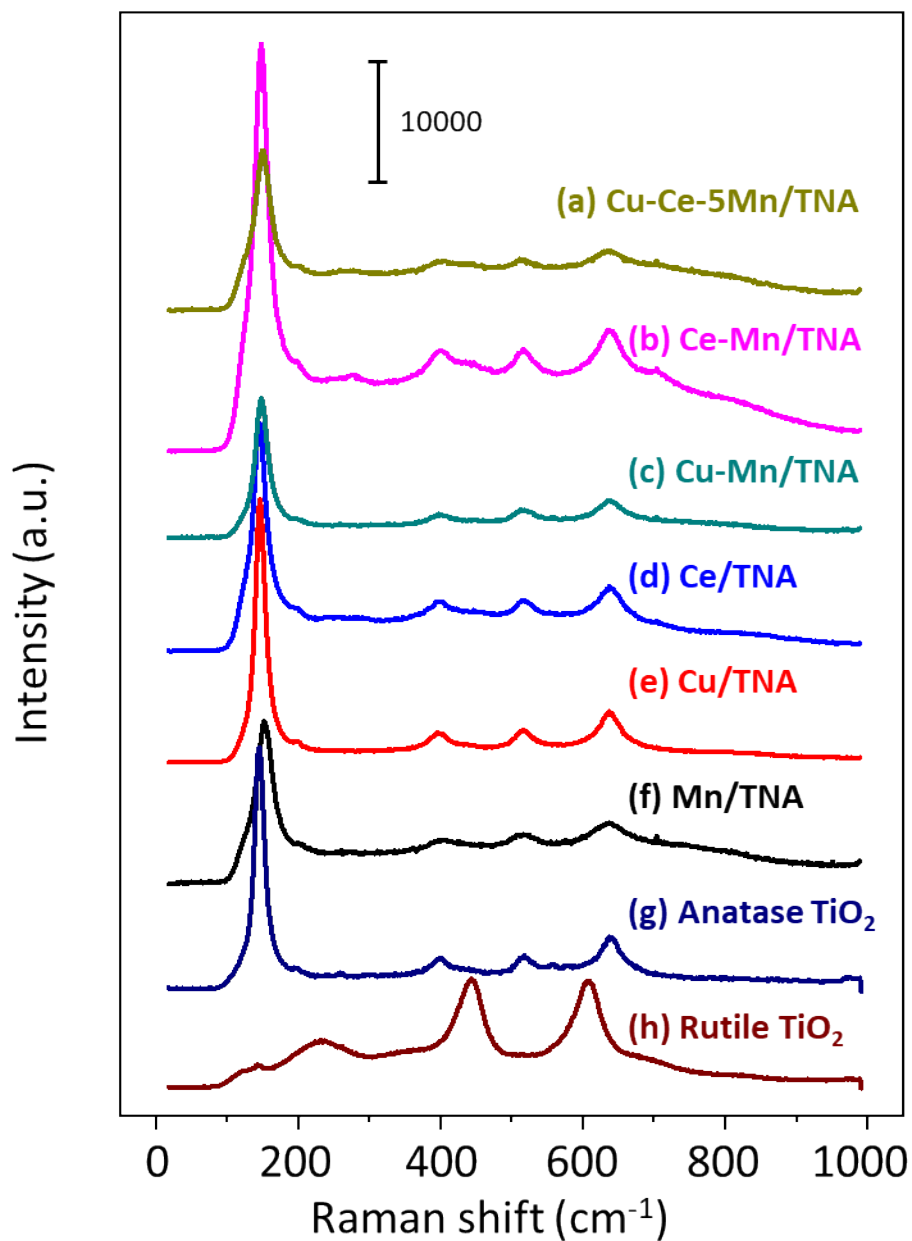
2.2 Structural Characterization

Figure S5. Raman spectra of the transition metal doped nanoarray catalysts: (a) 9-2_100Cu-Ce-5Mn/TNA, (b) 5-9_100Ce-Mn/TNA, (c) 5-7_100Cu-Mn/TNA, (d) 3-9_100Ce/TNA, (e) 3-7_100Cu/TNA, (f) 3-3_100Mn/TNA, (g) Anatase TiO_2, (h) Rutile TiO_2.
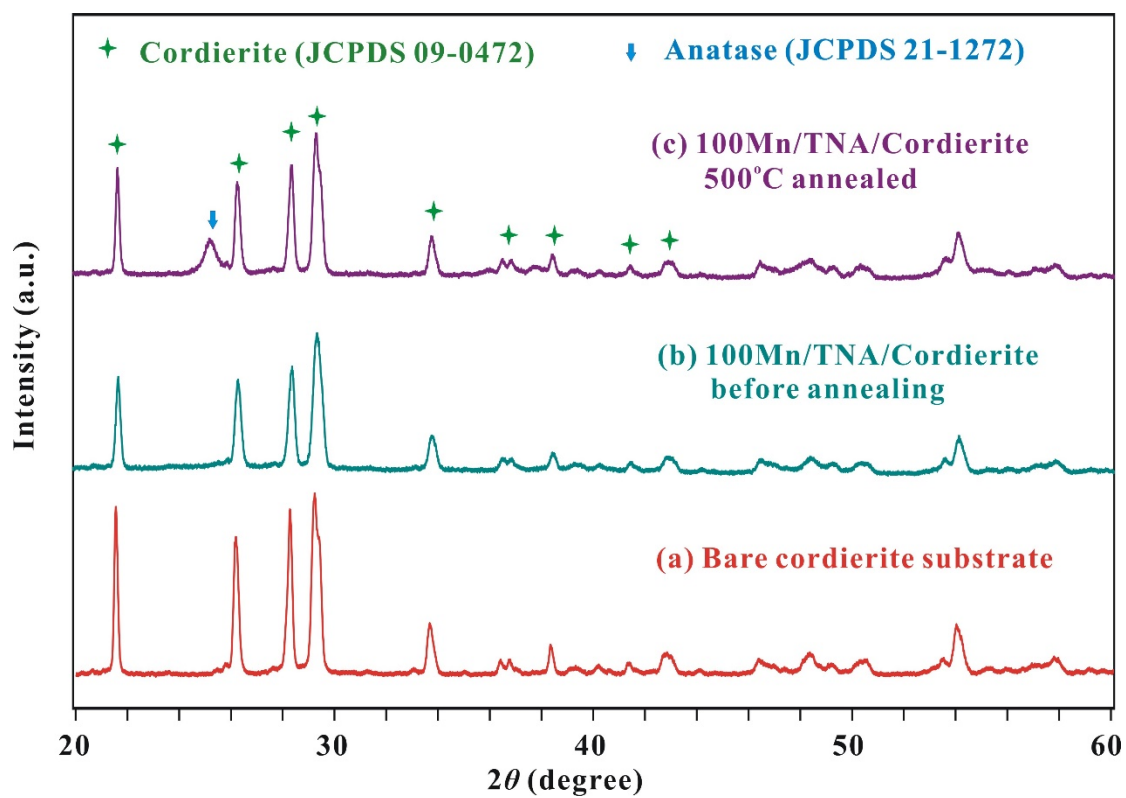
Figure S6. XRD patterns of the 100Mn/TNA sample (b) before and (c) after the calcination at 500°C as well as (a) the bare cordierite substrates
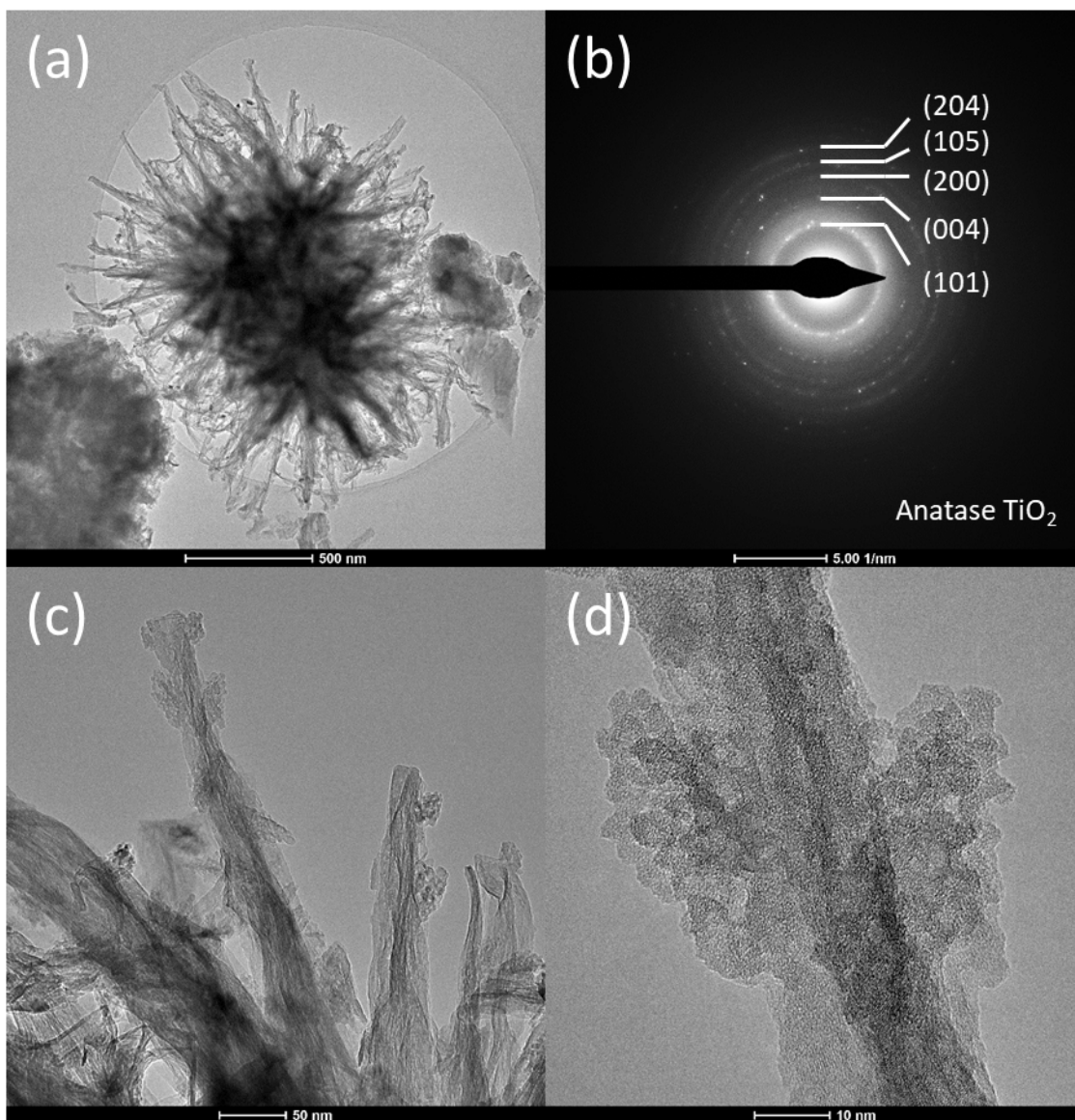
Figure S7. The (a) and (c) BF images, (b) SAED pattern and (d) HRTEM image of the Ce doped TiO$_2$ nanoarray (TNA) catalysts, 3-9_100Ce/TNA. The distinctive diffraction rings can be indexed by Anatase TiO$_2$ (JSPDS 21-1272).
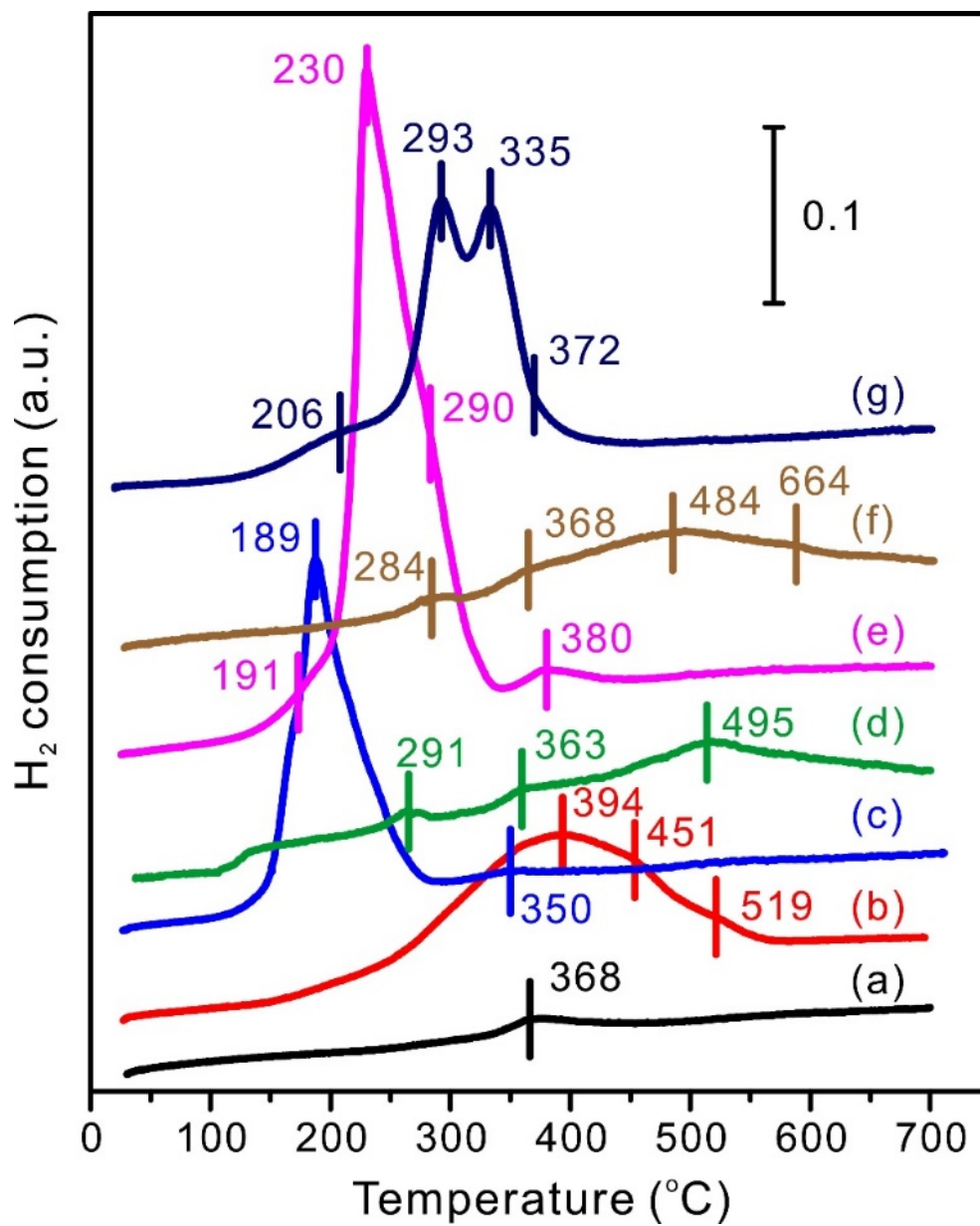
2.3 Catalyst Reducibility

Figure S8. H_2-TPR profile for (a) blank TiO_2, (b) 100Mn/TNA, (c) 100Cu/TNA, (d) 100Ce/TNA, (e) 100-Cu-Mn/TNA, (f) 100-Ce-Mn/TNA and (g) 100-Cu-Ce-Mn/TNA.

For the blank TiO_2 nanoarrays, there is only one reduction peak at 368 °C with quite low intensity (**Fig. S8a**), which is ascribed to the reduction of the surface capping oxygens on the TiO_2 surfaces.[3, 4] Therefore, the H_2 consumption in the other samples result from the reduction of the other species.

The monometallic Mn/TNA catalyst (**Fig. S8b**) exhibits a broad reduction peak, which can be split into three peaks at 394, 451 and 519 °C corresponding to the reductions of Mn^{4+} to Mn^{3+}, Mn^{3+} to $Mn^{2.67+}$ and $Mn^{2.67+}$ to Mn^{2+}, respectively.[5, 6] The broad reduction peak results from the complete intercalation of the Mn atoms into the TiO_2 lattice without phase segregation, making the reduction of the manganese species occur gradually in a wide temperature range instead of showing sharp reduction peaks.

The reduction profile of the 100Cu/TNA catalyst exhibits two broad peaks at 189 and 350 °C, which can be ascribed to the reduction of the Cu^{2+} to Cu^{1+}, in particular to the isolated copper atoms, and the monovalent copper species, respectively (**Fig. S8c**).[7, 8]

The 100Ce/TNA catalyst shows two weak peaks at 291, 363 °C and one broad peak at 495 °C (**Fig. S8d**), which can be assigned to the reduction of the amorphous ceria on the TiO_2 nanoarray surfaces ($T_1 = 291$ °C, Ce^{4+}-O-Ce^{4+}), the surface capping oxygen on the TiO_2 surface ($T_2 = 363$ °C),[3, 4] and the bulk CeO_2 ($T_3 = 495$ °C),[9, 10] respectively. The low intensity of the third peak reveals a high dispersion of ceria on the support avoiding large agglomerates which is in accordance with the XRD results that no CeO_2 crystalline phases are detectable.[7, 11]

When Cu and Mn were combined, four reduction peaks are observed over the 100Cu-Mn/TNA catalyst at 191, 230, 290 and 380 °C, respectively (**Fig. S8e**). The broad peak

centered at 191 °C (T_1) can be attributed to the reduction of CuO particles having strong interaction with the TiO_2 support, while the sharp reduction peak centered at 230 °C (T_2) is mainly due to the reduction of CuO particles having little or no interaction with the support.[8, 12] There is a shoulder peak on the right side of the T_2 peak centered at ~290 °C (T_3), which can be assigned to the reduction of MnO_2 to Mn_2O_3. The broad peak at 380 °C (T_4) is possible to correspond to the reduction of Mn_2O_3 species. Compared to the reduction profile of 100Mn/TNA, the intensity of the reduction peak of MnO_2 to Mn_2O_3 (T_3) increased significantly, indicating the increased Mn^{4+}/Mn^{3+} ratio in the 100Cu-Mn/TNA catalyst (**Table 1**). Furthermore, the total H_2 consumption of the 100Cu-Mn/TNA catalyst is much higher than that of the 100Cu/TNA and 100Mn/TNA catalysts, and the peak temperature also decreases from 394 to 290 °C. All these observations help to explain the enhanced low-temperature catalytic activity of the Cu-doped samples because the total H_2 consumption is an indicator of the low temperature reactivity of the catalysts.

Compared with the enhanced H_2 consumption over the Cu-Mn/TNA catalysts (3,504 μmole/g), the Ce-Mn/TNA catalyst exhibits a broad and weak peak from 200 to 700 °C with a decreased H_2 consumption of 1322 μmole/g (**Fig. S8f** and **Table 1**). More specifically, the broad reduction peak can be fitted into one broad peak at 484 °C (T_3), and three small peaks centered at 284 (T_1), 368 (T_2) and 664 °C (T_4), respectively, which can be assigned to the reduction of the Mn species and the reduction of amorphous ceria on the TiO_2 surfaces (Ce^{4+}-O-Ce^{4+}), the surface capping oxygen [3, 4], and the (Ce^{3+}-O-Ce^{4+}) of bulk CeO_2, respectively.[9, 10] Compared with the pure Mn/TNA

and Ce/TNA catalysts, the reduction temperatures of all the species in the bimetallic Ce-Mn/TNA catalysts increase correspondingly.

Finally, the H_2-TPR profile of the trimetallic Cu-Ce-Mn/TNA catalyst combines the properties of the mono- and bimetallic catalysts, and four distinctive peaks are identified in **Fig. S8g**, including the reduction of CuO particles being in strong ($T_1 = 206\ °C$) and little ($T_2 = 293\ °C$) interactions with the TiO_2 supports,[8, 12] and the reduction of MnO_2 ($T_3 = 335\ °C$) and Mn_2O_3 ($T_4 = 372\ °C$), respectively. Compared to Cu-Mn/TNA, the reduction temperatures of T_1, T_2, and T_3 of the Cu-Ce-Mn/TNA catalysts increased correspondingly. The total H_2 consumption of the Cu-Ce-Mn/TNA catalyst (2,123 μmole/g) is also lower than that of the Cu-Mn/TNA (3,504 μmole/g), which is due to the introduction of Ce element.
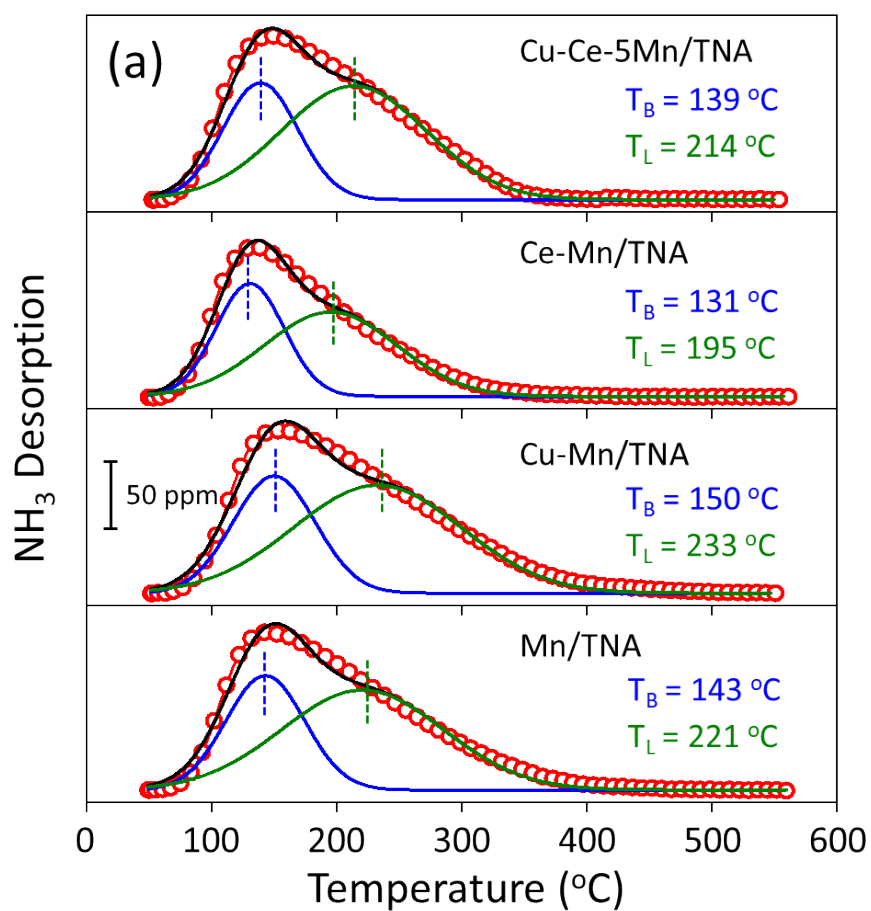
2.4. Surface Adsorption and Desorption

Figure S9. (a) NH_3-TPD profiles and (b) quantified NH_3 adsorption capacity and ratio between the Lewis and Brønsted acid sites over the selected catalysts.
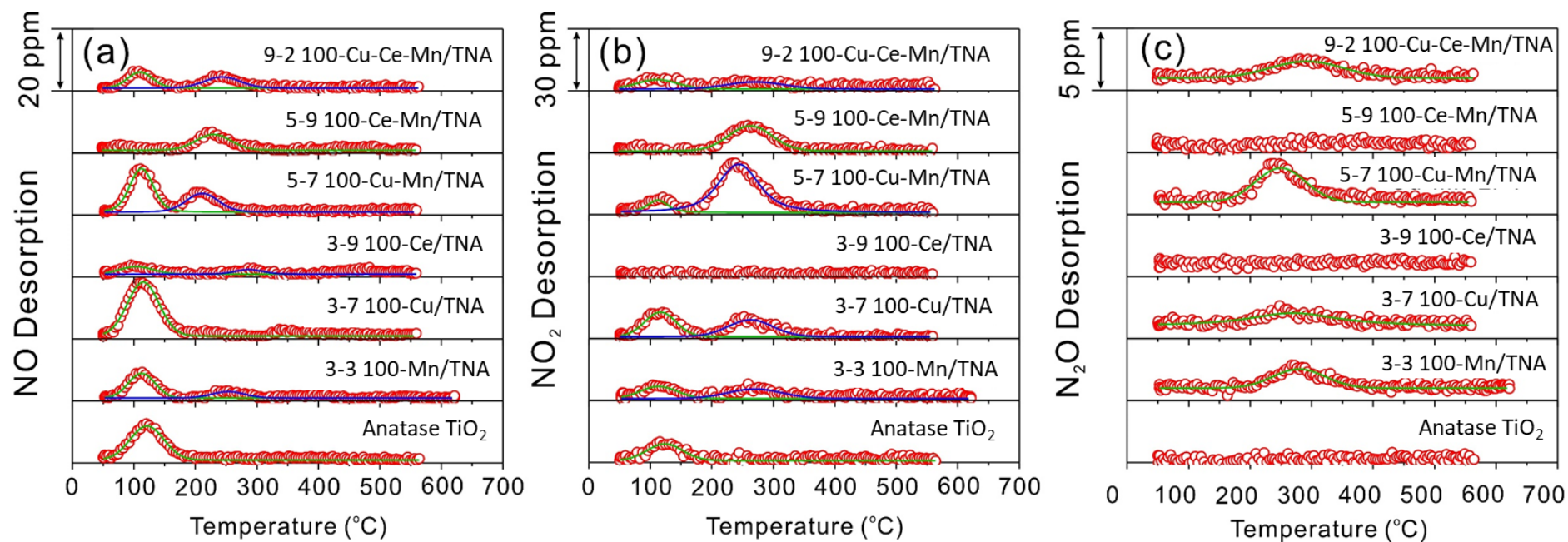
Figure S10. Desorption profiles of different NO_x species during the NO-TPD tests on selected catalysts using FTIR. (a) NO profiles, (b) NO_2 profiles, (c) N_2O profiles.

2.5. *In situ* DRIFTS and Reaction Mechanism Study
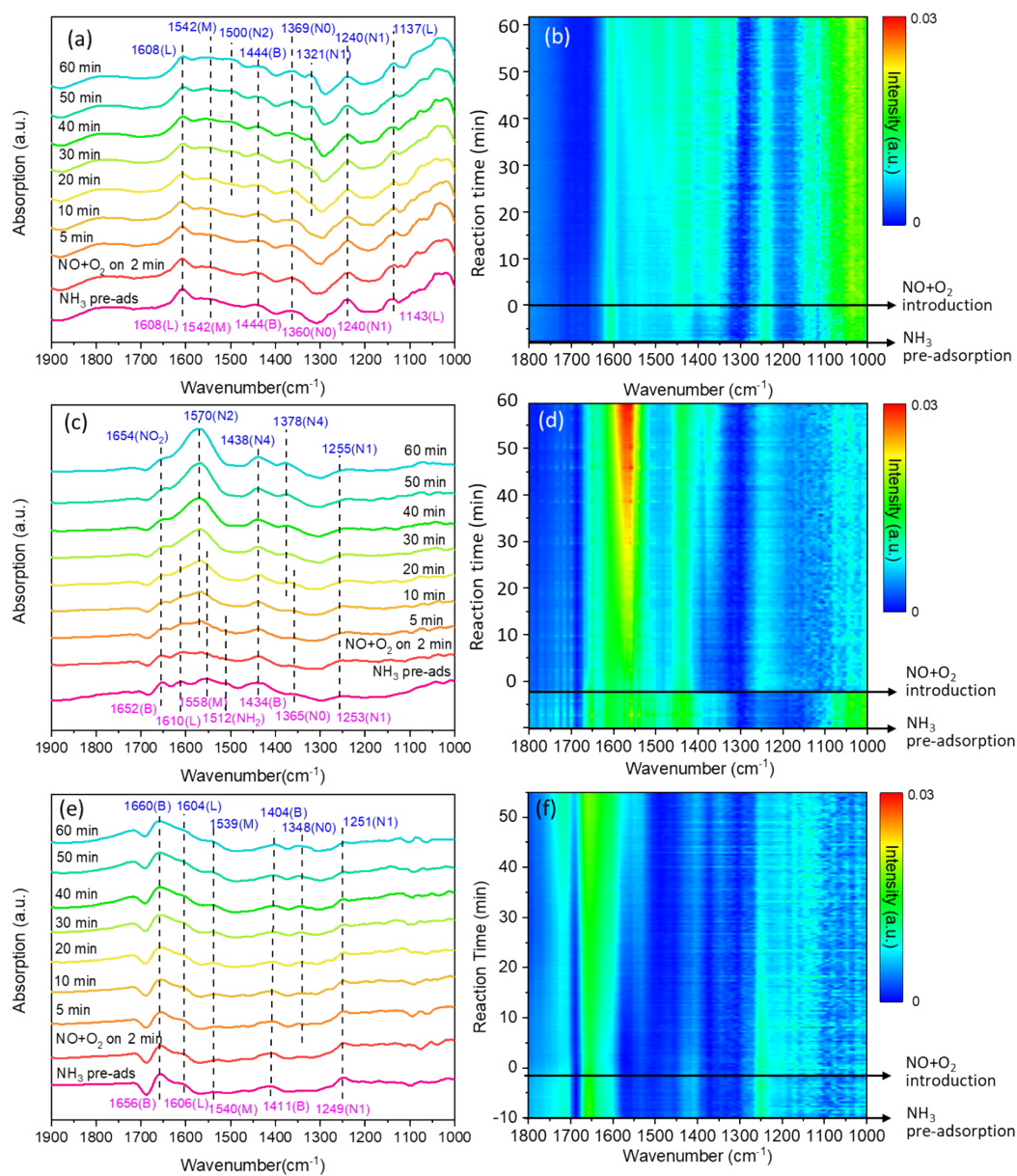

Figure S11. *In situ* DRIFT spectra of NO + O$_2$ reacted with pre-adsorbed NH$_3$ species at 150 °C over (a, b) Mn/TNA, (c, d) Cu-Mn/TNA and (e, f) Ce-Mn/TNA. Conditions: [NO] = [NH$_3$] = 500 ppm, [O$_2$] = 5 vol.% (when used) and N$_2$.

The *in situ* FTIR spectra of the surface reactions between NO + O_2 and the pre-adsorbed NH$_3$ species at 150 °C over the selected catalysts of Mn/TNA, Cu-Mn/TNA, Ce-Mn/TNA and Cu-Ce-5Mn/TNA are summarized in **Fig. S11**. As shown, when NH$_3$ was firstly introduced, the surfaces of all the selected catalysts were quickly covered by the NH$_3$-derived species, including the NH$_3$ coordinated on Lewis acid sites (L) at 1604-1610 and 1041-1143 cm^{-1} [13, 14], the NH$_4^+$ bounded to Brønsted acid sites (B) at 1434-1444 and 1652-1656 cm^{-1} [14, 15], the NH$_3$ oxidation intermediates (M) at 1540-1558 cm^{-1} [16], the free nitrate ions (N0) at 1360-1365 cm^{-1} [17], and the monodentate nitrates (N1) at 1240-1253 cm^{-1} [14, 18]. Furthermore, the IR band for the -NH$_2$ groups [19] at 1512 cm^{-1} is detectable over the Cu-Mn/TNA catalyst in **Fig. S11c**, indicating the oxidation of the adsorbed NH$_3$ on the surface, which helps to explain the excellent low temperature activity of the Cu-Mn/TNA catalyst. Meanwhile, the pre-adsorption of NH$_3$ led to the weak IR bands Ce doped catalyst in **Fig. S11e**, which agrees with the low adsorption capacity of Ce-Mn/TNA catalyst illustrated in **Fig. 6**. After NO and O_2 were introduced subsequently, different catalysts exhibited various activities towards the surface reactions between the NO + O_2 and the pre-adsorbed NH$_3$ species.

For the monometallic Mn/TNA catalyst in **Fig. S11a** and **b**, no significant changes were observed in the original pre-adsorbed species with only a slight decrease in the IR band intensity of Lewis acid sites (L) at 1608 cm^{-1}. Meanwhile, a few new species became detectable with the co-adsorption of NO and O_2, including the bidentate nitrate (N2) at 1500 cm^{-1} [14] and new adsorption sites of (N1) at 1321 cm^{-1}. The evolution in the FTIR spectra indicates that the pre-adsorbed NH$_3$ did not hinder the adsorption of the NO +

O_2 and the formation of adsorbed NO_x species over Mn/TNA catalyst.

For the bimetallic Cu-Mn/TNA catalyst, vigorous surface reactions were observed after the introduction of NO and O_2. As shown in **Fig. S11c and d**, the NH_3 coordinated on Lewis acid sites (L), the NH_3 oxidation intermediates (M) and the free nitrate ions (N0) were quickly consumed in the first 20 min, and the $-NH_2$ groups were consumed in only 5 min. The IR bands of the NH_4^+ bounded to Brønsted acid sites (B) were also quickly covered by the peaks of NO_2 at 1654 cm^{-1} and the linear nitrite (N4) at 1438 cm^{-1} [20]. The IR band for the monodentate nitrates (N1) at 1253 cm^{-1} remained unchanged throughout the experiments, indicating that the monodentate nitrates (N1) are not the active intermediates during the SCR-NH_3 process. Meanwhile, with the co-contact of NO and O_2, IR bands for bidentate nitrate (N2) at 1570 cm^{-1} [14] and the linear nitrite (N4) at 1378 cm^{-1} [20] quickly became intensified, and the surface of the Cu-Mn/TNA catalysts were quickly saturated with the absorbed NO_x species.

The bimetallic Ce-Mn/TNA catalyst did not exhibit surface reaction activity upon the introduction of NO and O_2 at 150 °C. As displayed in **Fig. S11e and f**, all the existing pre-adsorbed species remained unchanged and only the free nitrate ions (N0) showed up at 1348 cm^{-1} [17]. The absence of other NO_x species indicates that the introduction of Ce can prohibit the adsorption of NO and O_2 with the catalyst surface saturated with the pre-adsorbed NH_3-derived species over the Ce-Mn/TNA catalyst.
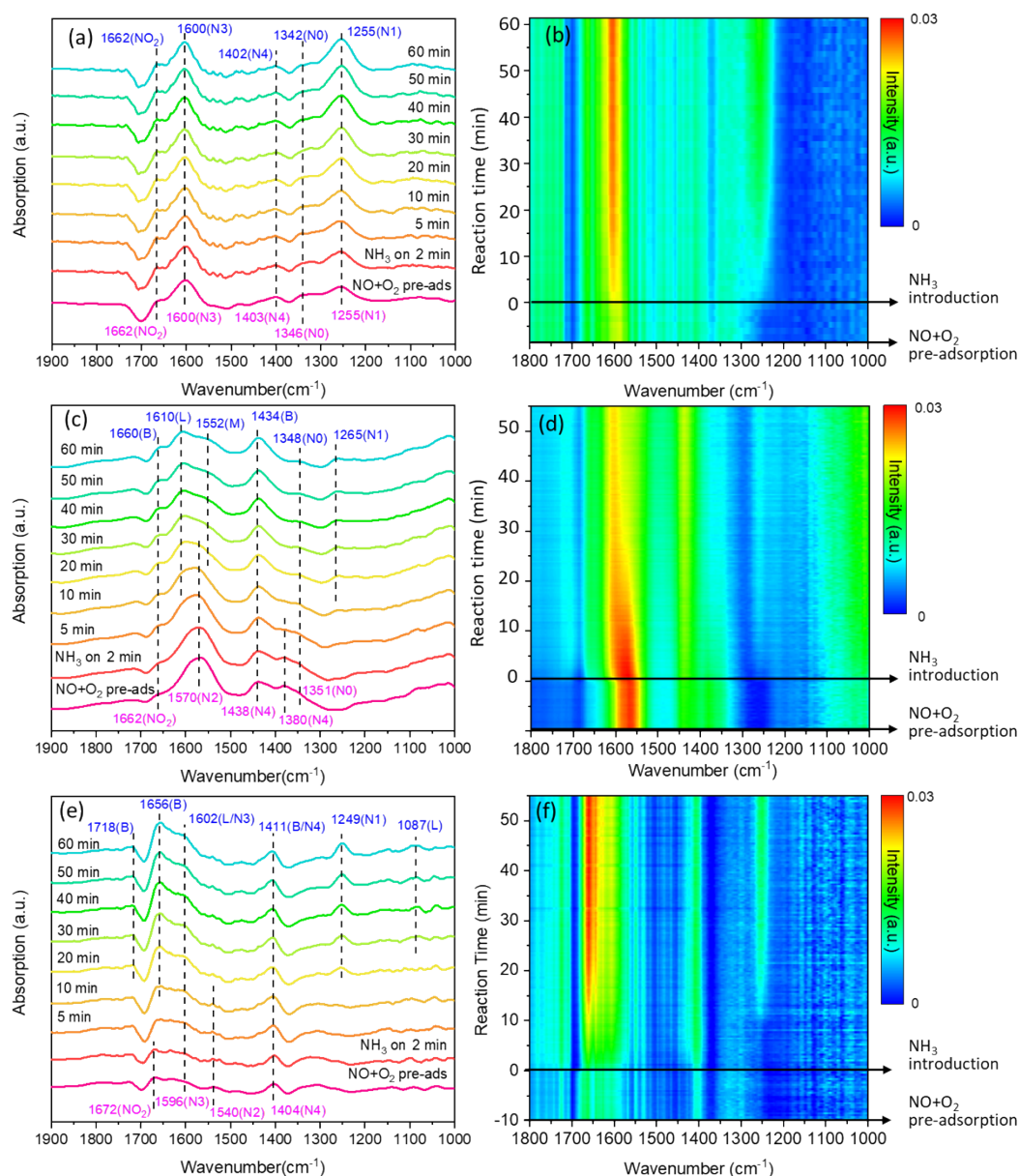
Figure S12. *In situ* DRIFT spectra of NH_3 reacted with pre-adsorbed NO_x species at 150 °C over (a, b) Mn/TNA, (c, d) Cu-Mn/TNA and (e, f) Ce-Mn/TNA. Conditions: $[NO] = [NH_3] = 500$ ppm, $[O_2] = 5$ vol.% (when used) and N_2.

When the reactant was introduced in a reverse order, the *in situ* FTIR spectra of the surface reactions between NH_3 and the pre-adsorbed NO_x species at 150 °C over the selected catalysts are summarized in **Figure S12**. The co-adsorption of NO and O_2 led to the coverage of the catalyst surfaces by the NO_x species, including the NO_2 at 1658-1672 cm^{-1}, the bidentate nitrate (N2) at 1540-1581 cm^{-1} [14], the free nitrate ions (N0) at 1344-1346 cm^{-1} [17], the monodentate nitrates (N1) at 1255 cm^{-1} [14, 18], the bridging nitrates (N3) at 1596-1600 cm^{-1} [21], and the linear nitrite (N4) at 1404-1438 cm^{-1} [20]. The evolution of the *in situ* DRIFTS spectra upon the introduction of NH_3 helps to elucidate the surface reaction intermediates and pathways from another perspective.

For the monometallic Mn/TNA catalyst, unlike the surface reactions between the NO and NO_2 with pre-absorbed NH_3, no obvious changes in these original pre-absorbed species nor new NH_3-derived species were observed in the IR bands when NH_3 was introduced to the pre-adsorbed NO_x species covered Mn/TNA sample, as displayed in **Figure S12a** and **b**. Therefore, the pre-adsorbed NO_x species prohibits the adsorption of NH_3 over the Mn/TNA catalyst surfaces. The different IR band evolutions in **Fig. S11a** and **Figure S12a** when NO and NH_3 were introduced in different sequences indicate that the NH_3-SCR reaction occurs only when the NH_3-derived species are pre-absorbed over the Mn/TNA catalyst surface. Furthermore, the incomplete consumption of the NH_3 coordinated on Lewis acid sites (L) explains the low NO conversion rate over the Mn/TNA catalyst at 150 °C.

When NO and O_2 were pre-absorbed on the Cu-Mn/TNA catalyst surface and NH_3 was introduced subsequently, the evolution of the FTIR spectra was almost reversed. As

shown in **Figure S12c** and **d** when NH_3 was introduced, the absorbed NO_2 and bidentate nitrate (N2) were quickly consumed in 5 and 20 min, respectively. The catalyst surface was finally dominated with the NH_3 derived species namely the NH_3 coordinated on Lewis acid sites (L) at 1602 cm^{-1} and 1087 cm^{-1} [13, 14], the NH_4^+ bounded to Brønsted acid sites (B) at 1718 cm^{-1}, 1656 cm^{-1} and 1411 cm^{-1} [14, 15] and the monodentate nitrates (N1) at 1249 cm^{-1} [14, 18]. The quick consumption of the absorbed species over the Cu-Mn/TNA catalyst reveals that Cu can greatly facilitate the adsorption and reaction at low temperature. Especially, the inert NH_4^+ species bounded to Brønsted acid sites (B) were also activated by adding Cu into the Mn based catalysts.

For the Ce doped bimetallic Ce-Mn/TNA catalyst, the surface reactions were quite different when NO and NH_3 were introduced in different orders. As exhibited in **Figure S12e** and **f**, when NO and O_2 were pre-adsorbed and NH_3 was introduced subsequently, the NO_2 and bidentate nitrate (N2) were quickly consumed in 5 and 10 min, respectively. The quick consumption of the pre-adsorbed NO_x species and saturation by the NH_3-derived species is due to the low NO_x adsorption capacity of the Ce-doped catalysts, as was demonstrated by the NO-TPD tests. The prohibited adsorption of NO_x species leaves the surfaces of the Ce-Mn/TNA catalyst intact and ready for the adsorption of NH_3, which helps to explain the different evolution features of FTIR spectra over the Ce-Mn/TNA catalyst with different reactant pre-adsorbed.

Reference

1.   X. Lu, S. Hoang, W. Tang, S. Du, S. Wang, F. Liu, W. Zhong, S. L. Suib, G. Yang, F.-Y. Zhang and P.-X. Gao, *ACS Applied Materials & Interfaces*, 2018, **10**, 35164-35174.

2.   Aftertreatment Protocols for Catalyst Characterization and Performance Evaluation: Low Temperature Oxidation Catalyst Test Protocol. http://cleers.org/ltat-protocols (accessed date Dec 22, 2016).

3.   S. Watanabe, X. Ma and C. Song, *The Journal of Physical Chemistry C*, 2009, **113**, 14249-14257.

4.   S. Kuhaudomlap, O. Mekasuwandumrong, P. Praserthdam, S.-I. Fujita, M. Arai and J. Panpranot, *Catalysts*, 2018, **8**.

5.   B. Thirupathi and P. G. Smirniotis, *Journal of Catalysis*, 2012, **288**, 74-83.

6.   P. Suktha, N. Phattharasupakun, P. Dittanet and M. Sawangphruk, *RSC Advances*, 2017, **7**, 9958-9963.

7.   T. Boningari, D. K. Pappas and P. G. Smirniotis, *Journal of Catalysis*, 2018, **365**, 320-333.

8.   F. Boccuzzi, A. Chiorino, G. Martra, M. Gargano, N. Ravasio and B. Carrozzini, *Journal of Catalysis*, 1997, **165**, 129-139.

9.   B. Murugan and A. V. Ramaswamy, *The Journal of Physical Chemistry C*, 2008, **112**, 20429-20442.

10.   X. Gao, Y. Jiang, Y. Fu, Y. Zhong, Z. Luo and K. Cen, *Catalysis Communications*, 2010, **11**, 465-469.

11.   L. Chen, D. Weng, Z. Si and X. Wu, *Progress in Natural Science: Materials International*, 2012, **22**, 265-272.

12.   B. Thirupathi and P. G. Smirniotis, *Applied Catalysis B: Environmental*, 2011, **110**, 195-206.

13.   H. Jiang, L. Zhang, J. Zhao, Y. Li and M. Zhang, *Journal of Materials Research*, 2016, **31**, 702-712.

14.   Z. Fan, J.-W. Shi, C. Gao, G. Gao, B. Wang, Y. Wang, C. He and C. Niu, *Chemical Engineering Journal*, 2018, **348**, 820-830.

15.   L. Xu, X.-S. Li, M. Crocker, Z.-S. Zhang, A.-M. Zhu and C. Shi, *Journal of Molecular Catalysis A: Chemical*, 2013, **378**, 82-90.

16.   P. R. Ettireddy, N. Ettireddy, T. Boningari, R. Pardemann and P. G. Smirniotis, *Journal of Catalysis*, 2012, **292**, 53-63.

17.   R. Jin, Y. Liu, Y. Wang, W. Cen, Z. Wu, H. Wang and X. Weng, *Applied Catalysis B: Environmental*, 2014, **148-149**, 582-588.

18.   L. Zhang, L. Shi, L. Huang, J. Zhang, R. Gao and D. Zhang, *ACS Catalysis*, 2014, **4**, 1753-1763.

19.   D. Sun, Q. Liu, Z. Liu, G. Gui and Z. Huang, *Applied Catalysis B: Environmental*, 2009, **92**, 462-467.

20.   D. Meng, W. Zhan, Y. Guo, Y. Guo, L. Wang and G. Lu, *ACS Catalysis*, 2015, **5**, 5973-5983.

21.   J. Liu, X. Li, Q. Zhao, J. Ke, H. Xiao, X. Lv, S. Liu, M. Tadé and S. Wang, *Applied Catalysis B: Environmental*, 2017, **200**, 297-308.